

A Posterior MWPM Decoding Boosts the XYZ Planar Code

Zhiwei Wang¹ and Liqi Wang¹

¹School of Mathematics, Hefei University of Technology, 230601 Hefei, China

May 25, 2026

Abstract

The minimum-weight perfect matching (MWPM) decoder is a standard decoding strategy for surface codes, but its performance degrades considerably under biased noise. In this paper, a modified surface code, termed the XYZ planar code, is introduced, and the MWPM decoder is extended to posterior MWPM (pMWPM) with almost no increase in decoding complexity. The XYZ planar code exhibits higher and more stable thresholds than the planar code under almost all bias conditions, while also achieving significantly lower logical error rates. Specifically, in the infinite-bias case, the threshold of the XYZ planar code is improved by about 36% compared to that of the surface code, and it maintains comparable or higher thresholds under other biases—for example, the threshold reaches approximately 15.5% at bias $\eta = 1$ and 14.2% at $\eta = 100$. Furthermore, pMWPM can be adapted to a wide range of modified surface codes, and the results presented in this work also indicate its excellent potential in other scenarios, such as configurations in which Y operators involve a larger number of data qubits.

1 INTRODUCTION

Quantum error correction (QEC) stands as a critical enabler for the realization of scalable, fault-tolerant quantum computation. Among various QEC codes, the surface code [1, 2] has emerged as a leading candidate due to its high error threshold and compatibility with local interactions in two-dimensional architectures. However, its performance is typically optimized for symmetric noise models, such as depolarizing noise, which may not accurately reflect the physical noise characteristics in many experimental platforms. Notably, in systems like superconducting qubits [3], quantum dots [4], and trapped ions [5] noise is often biased, with dephasing errors occurring at a significantly higher rate than bit-flip errors.

Recent research indicates that tailoring surface code variants for biased noise yields significant benefits, where bias is defined as the ratio of the probability of a high-rate Z error to the sum of the probabilities of low-rate X and Y errors. The XY surface code doubles the number of effective syndrome bits associated with dominant Z errors by measuring the product of Y operators around the surface rather than Z operators [6, 7]. The stabilizer of the XZZX surface code consists of the product of two X operators and two Z operators that are identical on each face [8]. Both XY surface and XZZX surface encodings are Clifford-deformed surface codes [9] exhibiting remarkably high thresholds, approaching or even saturating the hashing bound across a wide range of biases.

Information encoded using surface codes is typically decoded through various methods. The minimum-weight perfect matching (MWPM) decoder [10, 11] has been accelerated by modern implementations such as sparse blossom [12, 13] and fusion blossom [14], achieving near-linear expected complexity. The union-find (UF) decoder [15] offers nearly linear worst-case complexity and can be combined with belief propagation (belief-find) [16] to improve performance. The BPOSD decoder [17, 18] integrates belief propagation with ordered statistics decoding to mitigate the degeneracy problem, reaching thresholds comparable to MWPM. The tensor network (TN) decoder [7, 19] attains the highest threshold under depolarizing noise among the decoders discussed, but at a significantly higher computational cost. Other decoding methods include cellular-automaton decoders [20, 21], renormalization group decoders [22], neural-network decoders [24, 23], and MaxSAT decoders [25]. MWPM is considered as a strong candidate for real-time decoding due to its high threshold and near-linear average complexity enabled by modern implementations.

This paper proposes a modified surface code and an improved MWPM method tailored for this code, demonstrating outstanding performance under biased noise conditions. It draws inspiration from

existing approaches to modify surface codes and from the posterior weighting strategies of reweighted MWPM [26] or recursive MWPM [27]. Based on these findings, our modified planar code dynamically assigns weights according to the physical error rate and bias, thereby achieving stable and high thresholds. To demonstrate the effectiveness of this combined strategy, experimental results under various biased noise conditions reveal the outstanding performance of the modified planar code.

2 PLANAR CODE

In the field of quantum error correction, the surface code represents an important class of topological coding schemes [28]. Its physical implementation relies on the arrangement of qubits on a two-dimensional lattice and is realized through local interactions between nearest qubits. Surface codes come in various types, the most common of which is the planar code—the surface code for qubits on a square lattice [29, 30].

A planar code can be visually represented on a two-dimensional array of qubits, as shown in Fig. 1. The qubits are divided into two functionally distinct types: data qubits, represented by gray circles in Fig. 1, which store the computational quantum states; and measurement qubits, which are further categorized into two types— X -measurement qubits and Z -measurement qubits, depicted by green and yellow circles, respectively—used to detect errors on the data qubits. The interaction between measure-

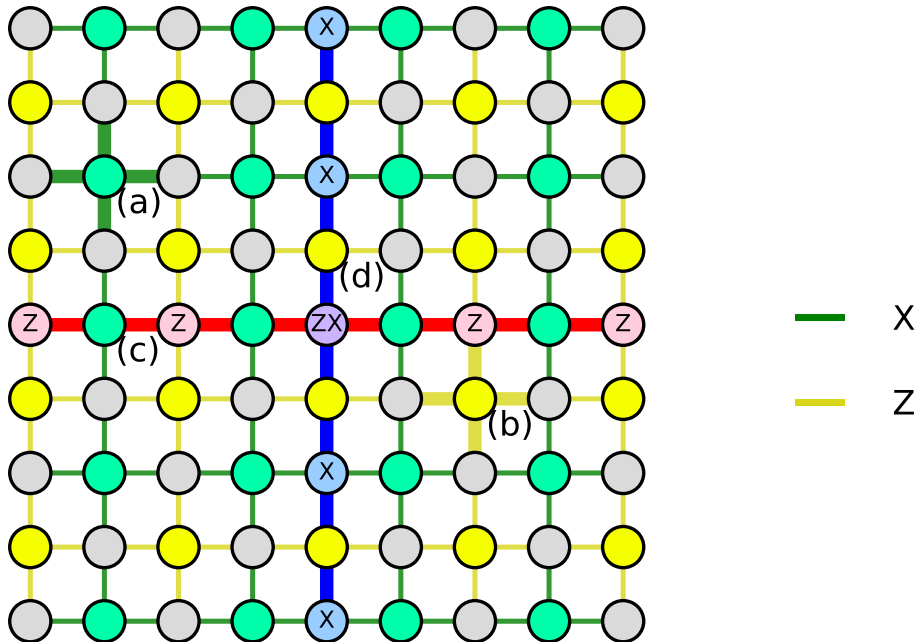


Figure 1: A schematic diagram of a 5×5 planar code. Data qubits, X -measurement qubits, and Z -measurement qubits are represented by gray, green, and yellow circles, respectively. The green and yellow lines indicate that the corresponding X or Z stabilizer measurements involve applying X or Z operators to their adjacent data qubits, respectively. In (a), an X -measurement qubit couples to its four adjacent qubits. In (b), a Z -measurement qubit involves its four nearest data qubits in the stabilizer measurement. (c) and (d) represent the logical Z operator and the logical X operator, respectively, which are formed by chains of Z or X operators spanning the lattice.

ment qubits and their neighboring data qubits is implemented through a series of Hadamard and CNOT gates, with the specific implementation depending on their positions on the lattice. Specifically, each measurement qubit is coupled to four data qubits, except on the boundaries where it is coupled to three.

As shown in (a) and (b) of Fig. 1, the X -measurement qubits apply X operators to their adjacent data qubits, while the Z -measurement qubits apply Z operators to their adjacent data qubits. The green lines and yellow lines indicate the types of Pauli operators applied by the measurement qubits to their connected data qubits. Each measurement forces its adjacent data qubits into an eigenstate of a specific operator product. For instance, a Z -measurement qubit forces its neighboring data qubits 1, 2, 3 and 4 into an eigenstate of the operator product $Z_1 Z_2 Z_3 Z_4$; hence, each Z -measurement qubit is said to

measure a Z stabilizer. Any pair consisting of one X -measurement qubit and one Z -measurement qubit must share an even number of data qubits; that is, they are connected to their common data qubits by an even number of lines of different colors. Consequently, by the anticommutation relation between the X and Z operators and the commutation relation between identical Pauli operators, all stabilizers commute with each other. For a planar code with distance d , there are $n = d^2 + (d - 1)^2$ data qubits and $n - 1$ measurement qubits (the stabilizer generators). Since each independent stabilizer generator reduces the degrees of freedom by one, the fact that there is one fewer measurement qubit than data qubits implies a two-dimensional code space, i.e., exactly one logical qubit is encoded. The distance d is defined as the minimum number of data qubits on which a nontrivial logical operator must act, which reflects the code’s error-correcting capability.

The measurement outcome of a measurement qubit provides partial information about the state of the neighboring data qubits to which it is coupled. If an odd number of adjacent data qubits suffer Pauli errors that anticommute with the operator applied by the measurement qubit, a non-trivial outcome is obtained. Conversely, if an even number of adjacent data qubits suffer such anticommuting Pauli errors, the outcome is trivial. The encoding process begins by performing projective measurements on all measurement qubits, thereby forcing all data qubits into a simultaneous eigenstate of all stabilizer generators—a state known as the quiescent state [30].

Besides the operators implemented by these measurement qubits, the planar code also supports logical operators that act nontrivially on the encoded information while preserving the code subspace. These logical operators are denoted as X_L , Y_L and Z_L , where $Y_L = Z_L X_L$. As illustrated in Fig. 1, X_L and Z_L can be viewed as specific paths traversing the lattice: a horizontal string of Z operators (red line) commutes with all stabilizers and thus forms a valid Z_L operator, while a vertical string of adjacent X operators (blue line) forms X_L . In the presence of noise, a logical error occurs when the combined effect of physical errors and the recovery operation implements a nontrivial logical operator.

From a mathematical perspective, as a stabilizer code, the planar code can be defined by an Abelian stabilizer group \mathcal{S} , whose codespace is the simultaneous $+1$ eigenspace of all operators in \mathcal{S} [12]. During error correction, a set of generators of \mathcal{S} (referred to as check operators) is measured to obtain the syndrome $\sigma(E)$ (a binary vector). If an error E commutes with a check operator, the corresponding syndrome entry is 0; if it anticommutes, the entry is 1. The decoder selects a correction operator R based on the syndrome, and decoding succeeds if $RE \in \mathcal{S}$. The planar code performs poorly in noise environments dominated by Z errors, yet even a minor modification to its Z stabilizers holds significant potential for performance enhancement.

3 XYZ PLANAR CODE

In the variant considered here, each Z stabilizer of the planar code is modified by replacing one Z operator with a Y operator at a single qubit position. Since the stabilizer measured by the measurement qubits consists of three distinct Pauli operators— X , Y and Z —this code is referred to as the XYZ planar code. Notably, it belongs to the non-CSS class [31].

In Figure 2, an example of a general XYZ planar code with distance $d = 5$ is shown. In this code, the X stabilizers remain unchanged (Figure 2(a)), still stabilizing four adjacent data qubits via X operators. All Z stabilizers are replaced by Z^2Y stabilizers or Z^3Y stabilizers, where Z^3Y denotes the product of three Z operators and one Y operator (i.e., $Z \otimes Z \otimes Z \otimes Y$). Because the Y operator anticommutes with X and Z , a data qubit located at a non-top-or-bottom boundary position of the lattice in the XYZ planar code must interact with Y operators from two different ZY stabilizers to preserve the commutativity of the stabilizers. Therefore, extending the XYZ planar code requires the vast majority of Z^2Y -measurement qubits or Z^3Y -measurement qubits to appear in pairs, such as those shown in Figure 2 (g) and (e) or (b) and (f), so that they can measure a larger number of data qubits. This is precisely the construction adopted in Fig. 2. All stabilizers measured by the measurement qubits in the figure satisfy Hermiticity and commute with each other, collectively defining the logical subspace of the code. This paper does not consider noisy gates or state preparation and measurement (SPAM) errors, so the choice of the initial state is unimportant [16].

Specifically, X stabilizer measurements are sensitive to Z or Y errors on the data qubits, while ZY stabilizer measurements are sensitive to X or Y errors on two or three of its adjacent data qubits, and to either X or Z errors on the remaining one. This relationship is illustrated by the following anti-commutation relations:

$$\begin{aligned}
X_1 X_2 X_3 X_4 Z_4 |\psi\rangle &= -Z_4 X_1 X_2 X_3 X_4 |\psi\rangle, \\
X_1 X_2 X_3 X_4 Y_4 |\psi\rangle &= -Y_4 X_1 X_2 X_3 X_4 |\psi\rangle, \\
Z_1 Z_2 Z_3 Y_4 X_1 |\psi\rangle &= -X_1 Z_1 Z_2 Z_3 Y_4 |\psi\rangle, \\
Z_1 Z_2 Z_3 Y_4 Y_1 |\psi\rangle &= -Y_1 Z_1 Z_2 Z_3 Y_4 |\psi\rangle, \\
Z_1 Z_2 Z_3 Y_4 X_4 |\psi\rangle &= -X_4 Z_1 Z_2 Z_3 Y_4 |\psi\rangle, \\
Z_1 Z_2 Z_3 Y_4 Z_4 |\psi\rangle &= -Z_4 Z_1 Z_2 Z_3 Y_4 |\psi\rangle.
\end{aligned} \tag{1}$$

For a general distance d , the lattice structure of the XYZ planar code consists of $2d - 1$ rows, where both data qubits and measurement qubits are counted as the starting qubits for each row. All data qubits in rows $4i - 1$ (with $i = 1, 2, \dots, \lfloor (d-1)/2 \rfloor$) interact via Y operators (shown as purple lines) with the Z^2Y or Z^3Y stabilizers above and below them. Consequently, the total number of data qubits involved in the Y operators is $\lfloor (d-1)/2 \rfloor \cdot d$. When d is odd, this number becomes $(d^2 - d)/2$. The total number of data qubits in the XYZ planar code is the same as that of the planar code, namely $2d^2 - 2d + 1$; hence the proportion of data qubits affected by Y operators is $(d^2 - d)/(4d^2 - 4d + 2)$.

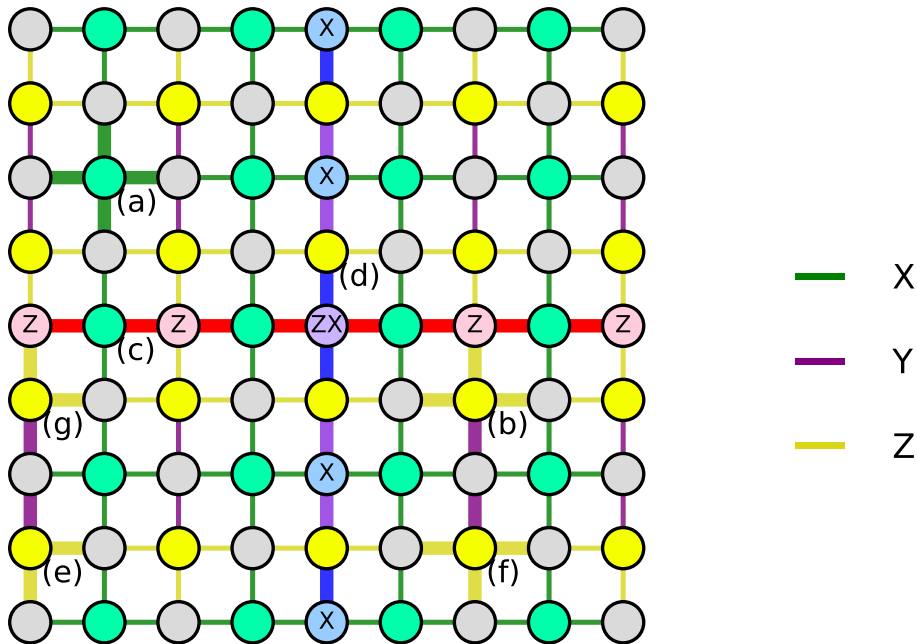


Figure 2: A schematic diagram of a 5×5 XYZ planar code. Data qubits, X -measurement qubits, and ZY -measurement qubits are represented by gray, green, and yellow circles, respectively. The green and yellow lines indicate that the corresponding X or ZY stabilizer measurements involve applying X or Z operators to their adjacent data qubits, respectively, while the purple lines indicate that the ZY stabilizer measurement involves a Y operator on its adjacent data qubit. In (a), an X -measurement qubit involves applying X operators to its four adjacent qubits. In (b) and (f), a ZY -measurement qubit involves applying Z operators to its three surrounding qubits and a Y operator on the data qubit directly below or above it. (c) and (d) represent the logical Z operator and the logical X operator, respectively, which commute with all stabilizers; the light purple lines in (d) are used to highlight the relationship between data qubits and adjacent ZY -measurement qubits. Unlike in the planar code, only specially chosen strings of Z operators spanning the lattice can serve as the logical Z operators of the XYZ planar code. In (e) and (g), a ZY -measurement qubit at the boundary involves applying Z operators to its two adjacent data qubits and a Y operator on the data qubit directly below or above it.

Under this distribution, the logical operators of the XYZ planar code are easy to determine. The XYZ planar code may no longer possess exactly the same logical operator structure as the planar code, but in special cases, similar to the planar code, the logical operators are strings of X or Z operators spanning the lattice, as shown in Figure 2 (c). Because none of the data qubits on that path are involved in any Y operator, the product of Z operators on these qubits forms a logical Z operator \bar{Z} . In contrast, the analogous product of Z operators on the data qubits of the next lower row—which originally formed the logical Z operator \bar{Z} in the planar code—no longer serves as a logical Z operator in the XYZ planar

code. This follows from the algebraic relation $Y = iXZ$, which implies that at each intersection, the Z operator in the original logical operator anticommutes with the Y operator in the stabilizer. For the same reason, the logical X operator \bar{X} can still be defined as the product of X operators on all data qubits along a vertical path connecting the top and bottom boundaries. Although the stabilizers of the XYZ planar code incorporate Y operators, by appropriately choosing paths such as those in Figure 2 (c) and (d), these logical operators commute with all stabilizers, including the ZY stabilizers.

In fact, many other distributions of ZY -measurement qubits are possible, leading to various distinct XYZ planar codes that form the XYZ planar code family.

4 MWPM DECODER

The minimum-weight perfect matching decoder is a standard choice for decoding surface codes. When an error occurs in quantum information encoded with a surface code, the MWPM method maps the resulting non-zero syndrome elements to vertices in a graph. It then identifies a set of edges (each with an associated weight) that are pairwise non-adjacent, such that the sum of their weights is minimized among all possible perfect matchings. A perfect matching is one that includes all vertices of the graph [10, 12]. This algorithm infers the most likely error based on the syndrome obtained from stabilizer measurements. Different errors may correspond to the same syndrome, and the goal of decoding is to select the error path that best matches the observed result—namely, the path with the minimum weight.

Decoding is typically performed separately for X and Z errors, X -measurement qubits and Z -measurement qubits are called Z and X checks, respectively, as they detect the corresponding errors. Taking Z errors as an example, consider a Z error $E \in \{I, Z\}^n$ in a stabilizer code. When each single-qubit operator Z anti-commutes with two X stabilizers in the planar code, the MWPM decoder can be applied. In this setting, a matching graph G_X is defined, where each node corresponds to an X stabilizer, and each edge between adjacent nodes corresponds to a single-qubit potential Z error. A set E of Z errors then corresponds to a subset of edges, and the syndrome $\sigma(E)$ is identified with the subset of nodes representing defects. The graph formed by these special nodes is called the Z -check subgraph. An analogous definition applies to the matching graph G_Z and the X -check subgraph. Decoding E is thus to find a minimum-weight set of edges whose associated boundary exactly matches the set of defect nodes. If the probability p_i of a Z error on qubit i varies, each edge can be assigned a weight $w_i = \log \frac{1-p_i}{p_i}$ [28], reflecting the likelihood of that error.

Define a binary noise vector \mathbf{e} such that $\mathbf{e}[i] = 1$ if the error occurs on qubit i , and 0 otherwise. The probability of error E occurring is

$$p(E) = \prod_i (1 - p_i)^{1 - \mathbf{e}[i]} p_i^{\mathbf{e}[i]}, \quad (2)$$

which satisfies

$$\log p(E) = \sum_i \log(1 - p_i) - \sum_i w_i \mathbf{e}[i]. \quad (3)$$

Hence, errors with higher probability correspond to smaller total edge weights [12].

One advantage of MWPM is that it always returns an error estimate consistent with the measured syndrome. In other words, when decoding the surface code with MWPM, the product RE always belongs either to \mathcal{S} or to $L\mathcal{S}$, where L is a logical operator. The former corresponds to successful decoding, while the latter indicates a decoding failure. Therefore, if the actual error differs from the estimated one, this does not necessarily mean that decoding has failed—if their difference is exactly a product of stabilizer elements, the correction procedure remains valid.

When the average physical error probability is below the threshold, the MWPM decoder performs well, and its performance improves as the code distance increases. Under perfect measurements, for the planar code, the threshold for a single subgraph (i.e., pure X or Z errors) is approximately 10.3%, while the threshold under the depolarizing noise model is about 15.5% [32]. The planar code tends to exhibit a higher logical failure rate and a lower threshold under biased noise, because the bias toward Z noise makes the Z -check subgraph denser, causing the probability threshold to be reached before the total physical error rate reaches the threshold of the depolarizing channel [33]. When the physical error rate exceeds the threshold, increasing the code distance of the planar code no longer enhances its performance.

The complexity of MWPM arises from two steps: constructing the syndrome graph (using Dijkstra’s algorithm) and finding a perfect matching (using the blossom algorithm). The Dijkstra step has complexity $O(n^2 \log n)$, where n is the number of data qubits, while the blossom step dominates with

$O(n^3 \log n)$. If equal weights are assumed, the graph can be built using Manhattan distance, but the overall runtime remains $O(d^6 \log d)$ [12], where d is the code distance.

5 POSTERIOR MWPM DECODER

Regard a Y error as a combination of an X error and a Z error. From the previous description of the XYZ planar code, the X stabilizer measurements are sensitive to Z errors, while the ZY -measurement qubits apply Z or Y operators to their adjacent data qubits, making the corresponding stabilizer measurements sensitive to both X and Z errors—with particular attention to Y and Z errors on the data qubits involved in the Y operator. In the following, an error (or operation) is said to cause a “flip” if it contributes

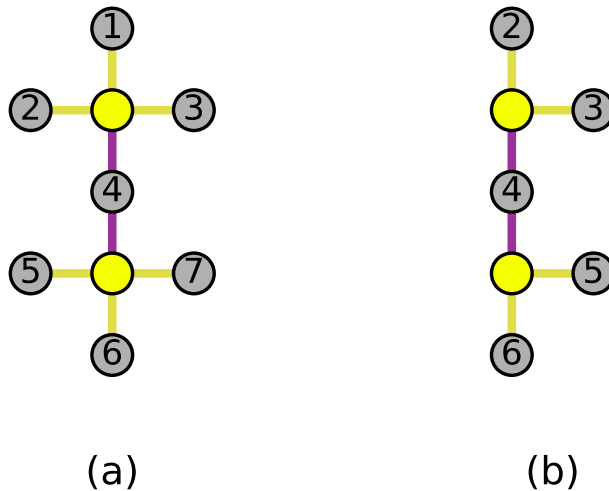


Figure 3: The structure of all ZY stabilizers in the XYZ planar code can be obtained by concatenating subfigures (a) and (b). In both subfigures (a) and (b), qubit 4 is simultaneously involved in the Y operators of two ZY stabilizers, and is therefore referred to as the central qubit, while the remaining qubits are called peripheral qubits.

non-trivially to the measurement outcome, and “no flip” otherwise. For example, when an odd number of data qubits adjacent to an X -measurement qubit suffer errors that cause flips (i.e., Z or Y errors), the measurement outcome undergoes a non-trivial change. Similarly, for a ZY -measurement qubit, the outcome undergoes a non-trivial change if the sum of the following is odd: the number of flips (i.e., X or Y errors) on the data qubits involved in the Z operator, plus the number of flips (i.e., X or Z errors) on the data qubit involved in the Y operator.

To exploit the sensitivity of ZY -measurement qubits to Z errors and thus improve the performance of the planar code when Z errors dominate, a special MWPM-based decoding scheme, termed posterior minimum-weight perfect matching (pMWPM), is designed.

In Fig. 3(a) and (b), the structures of interest are illustrated. Qubit 4 in Fig. 3 is called the central qubit; the remaining data qubits are called peripheral qubits. Under the assumption that the trivial and non-trivial change events between these structures are independent of one another, the posterior probability that qubit 4 suffers a Z or Y error, given the binary measurement outcomes $S_1, S_2 \in \{0, 1\}$ (0 = trivial change; 1 = non-trivial change) of its two adjacent measurement qubits, is computed. This posterior probability is then used to reweight qubit 4. Each data qubit independently suffers X , Y , or Z errors with probabilities p_x, p_y, p_z , total error probability $p = p_x + p_y + p_z$, and non-error probability $p_i = 1 - p$. The bias parameter $\eta = p_z / (p_x + p_y)$ with $p_x = p_y$ satisfies

$$p_x = p_y = \frac{p}{2(\eta + 1)}, \quad p_z = \frac{\eta p}{\eta + 1}. \quad (4)$$

The probability that any peripheral qubit flips its associated stabilizer measurement is $q = p_x + p_y$. Qubit 4 flips both stabilizer measurements if it suffers an X or Z error (probability $p_{\text{flip}} = p_x + p_z$), and flips none if it is idle or suffers a Y error (probability $p_{\text{noflip}} = p_i + p_y$).

Let the number of peripheral qubits per measurement qubit be n ($n = 2$ or 3 , corresponding to Fig. 3(b) and (a), respectively). Define

$$E_n = \begin{cases} (1-q)^2 + q^2, & n = 2, \\ (1-q)^3 + 3q^2(1-q), & n = 3, \end{cases} \quad O_n = \begin{cases} 2q(1-q), & n = 2, \\ 3q(1-q)^2 + q^3, & n = 3, \end{cases} \quad (5)$$

where $q = p_x + p_y$. Then the conditional probability that qubit 4 suffers a Z or Y error given the two measurement outcomes (S_1, S_2) is

$$P(Z \cup Y \mid S_1, S_2) = \begin{cases} p_y + p_z, & \text{if } S_1 \neq S_2, \\ \frac{p_z O_n^2 + p_y E_n^2}{p_{\text{noflip}} E_n^2 + p_{\text{flip}} O_n^2}, & \text{if } S_1 = S_2 = 0, \\ \frac{p_z E_n^2 + p_y O_n^2}{p_{\text{noflip}} O_n^2 + p_{\text{flip}} E_n^2}, & \text{if } S_1 = S_2 = 1, \end{cases} \quad (6)$$

with $p_{\text{noflip}} = 1 - p + p_y$ and $p_{\text{flip}} = p_x + p_z$. The prior weight is $w_{\text{prior}} = \ln \frac{1-(p_y+p_z)}{p_y+p_z}$, and the conditional weight is $w = \ln \frac{1-P}{P}$ for the corresponding probability P .

Algorithm 1: Decoding algorithm

Input: s_X : syndrome from X stabilizers,

s_{ZY} : syndrome from ZY stabilizers,

H_X : parity-check matrix for X stabilizers,

H_{ZY} : incidence matrix for ZY stabilizers, $2n$ columns; first n indicate X operators, last n indicate Z operators.

H_Y : first n columns of H_{ZY} ,

H_Z : last n columns of H_{ZY} ,

precomputed: structure containing conditional weights $w_{00}[k]$, $w_{11}[k]$, $w_{\text{diff}}[k]$ for $k = 2, 3$, and prior weight w_{prior} ,

group_size(j): function returning the number of peripheral qubits per ZY measurement for central qubit j (either 2 or 3).

Output: \hat{e}_Z, \hat{e}_X : estimated Z and X errors on data qubits.

1 Initialize weight vector w for Z -check subgraph: $w[j] \leftarrow w_{\text{prior}}$ for all j ;

2 **for** $j \leftarrow 1$ **to** n **do**

3 $I \leftarrow \{i \mid H_{ZY}[i][j] = 1\}$;

4 **if** $|I| = 2$ **then**

5 Let i_1, i_2 be the two indices in I ;

6 $k \leftarrow \text{group_size}(j)$;

7 $s_1 \leftarrow s_{ZY}[i_1]$, $s_2 \leftarrow s_{ZY}[i_2]$;

8 **if** $(s_1, s_2) = (0, 0)$ **then**

9 $w[j] \leftarrow \text{precomputed}.w_{00}[k]$;

10 **else**

11 **if** $(s_1, s_2) = (1, 1)$ **then**

12 $w[j] \leftarrow \text{precomputed}.w_{11}[k]$;

13 **else**

14 $w[j] \leftarrow \text{precomputed}.w_{\text{diff}}[k]$;

15 Construct G_X from H_X and w ;

16 $\hat{e}_Z \leftarrow \text{MWPM}(G_X, s_X)$;

17 Compute $\delta \leftarrow \hat{e}_Z \cdot H_Y^T \pmod{2}$;

18 $s'_Z \leftarrow s_{ZY} \oplus \delta$;

19 Construct G_Z from H_Z ;

20 $\hat{e}_X \leftarrow \text{MWPM}(G_Z, s'_Z)$;

21 **return** (\hat{e}_Z, \hat{e}_X)

All six conditional weights can be precomputed using the above formulas; the detailed derivation of the posterior probabilities is given in the Appendix. They are used to reweight the edges in the decoding graph according to the observed measurement outcomes. After reweighting, the Z -check subgraph is first decoded to obtain the Z errors. Then, for every central qubit where a Z error is decoded, the adjacent

ZY measurement outcomes are flipped, i.e., 1 is added modulo 2 to both S_1 and S_2 . Otherwise, no change is made. Subsequently, the X -check subgraph is decoded using conventional MWPM to obtain the X errors. This subgraph is called the X -check subgraph because after the flips, the ZY measurement symptoms are exactly those that would be caused by the expected X or Y errors. The detailed decoding procedure is presented in Algorithm 1, from which it follows that the error obtained from decoding must satisfy the syndromes s_X and s_{ZY} .

As will be shown in the results section, under varying degrees of Z -biased noise, pMWPM decoding achieves significantly lower logical failure rates and higher thresholds compared to MWPM decoding. This reduction in decoding error rate and enhancement of the threshold come at the cost of a negligible increase in decoding complexity. Both the MWPM decoder and the pMWPM decoder need to run the Blossom algorithm on a complete syndrome graph, which has $O(n)$ nodes and $O(n^2)$ edges. The complexity of both decoders is dominated by the Blossom algorithm and is $O(n^3 \log n)$ [12]. Although the pMWPM uses Dijkstra's algorithm to compute shortest paths, which adds a constant factor compared to the MWPM decoder that uses Manhattan distance, it does not change the asymptotic complexity order.

6 RESULTS

For each bias value $\eta \in \{0.5, 1, 3, 10, 30, 100, 1000, \infty\}$, the logical failure rate f is estimated using the pMWPM decoder. The sample mean error rate is obtained from 10^5 random trials for a range of physical error rates p near the threshold p_c , considering code distances $d \in \{35, 39, 43, 47\}$. To

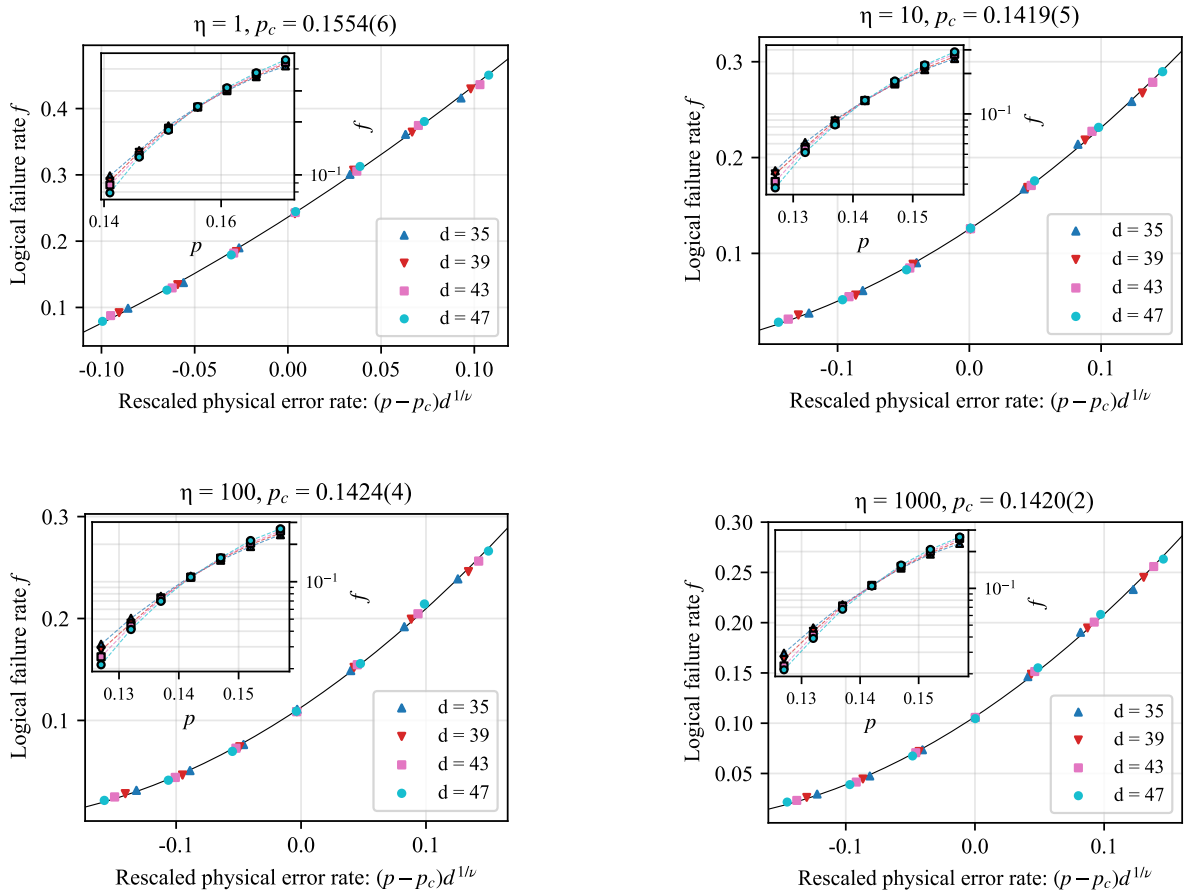


Figure 4: Logical failure rate f as a function of the rescaled error rate $x = (p - p_c)d^{1/\nu}$ for biases $\eta \in \{1, 10, 100, 1000\}$. The solid line is the best fit to the model $f = A + Bx + Cx^2$. The insets show the raw sample means over 100,000 runs for various values of p . Good agreement between the fitted model and the data is observed across all bias cases.

verify the effectiveness of the decoding strategy, Monte Carlo simulations of the XYZ planar code are

performed using pMWPM decoding across a range of biased channels. Stable threshold behavior is observed in all cases, with threshold values consistently falling between 14% and 16%, demonstrating the robustness of the pMWPM-decoded XYZ planar code. To obtain a more precise estimate of the threshold, the critical exponent method introduced in Ref. [34] is adopted. The scaling variable is defined as $x = (d/\xi)^{1/\nu} = (p - p_c)d^{1/\nu}$, and the failure rate is modeled by a truncated Taylor expansion around the critical point p_c . Specifically, a quadratic function $f = A + Bx + Cx^2$ is fitted to determine p_c , ν , and the nuisance parameters A , B , C . A detailed discussion of the validity range of this scaling approach is provided in Ref. [35].

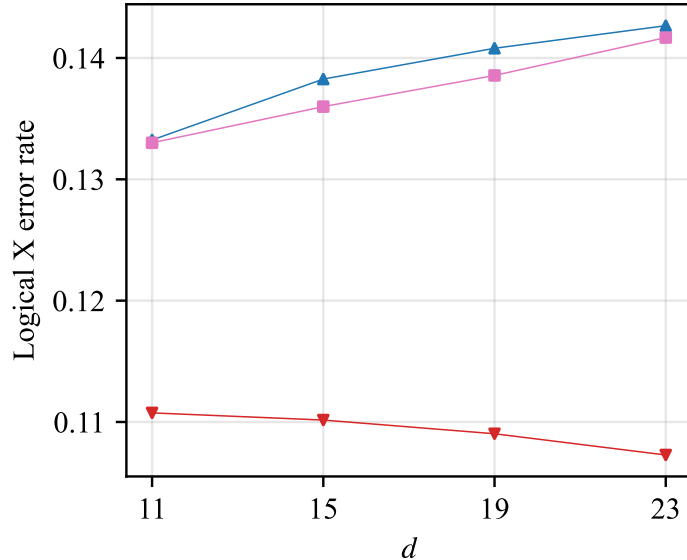


Figure 5: Under three different scenarios with the Z -checks subgraph density unchanged, the logical X error rate varies with the code distance d . As shown in the figure, the blue, pink, and red curves correspond to data qubit error rates of $(p_x = 0.001, p_y = 0.01, p_z = 0.13)$, $(p_x = 0.01, p_y = 0.001, p_z = 0.139)$, and $(p_x = p_y = 0.001, p_z = 0.139)$, respectively. It can be observed that in the first two cases, the logical X error rate increases with d , whereas in the latter case, it decreases with d . This indicates that increasing p_x and p_y errors has a negative impact on the threshold when the Z -check subgraph density remains unchanged.

The critical exponent method provides an estimate of p_c with low statistical uncertainty. However, it is worth noting that finite size effects [36] typically lead to a higher threshold estimate when smaller code distances are used. The threshold estimate is accurate only when the code distance d is much larger than the correlation length ξ . Given the practical limitations of classical computer simulations and the cost of measurements, moderate code distances d are employed to evaluate the threshold under high bias.

Under the biases considered in this work, the threshold of the XYZ planar code at $\eta = 1$ is very close to the peak threshold of the standard planar code under the depolarizing channel. For the pure dephasing channel, the threshold of the XYZ planar code is as high as 14.3%, representing an improvement of approximately 39% over the standard planar code. This performance advantage is maintained across most biases, with the XYZ planar code consistently achieving thresholds close to or above the optimal level of the standard planar code. The only exception occurs at $\eta = 0.5$, where the standard planar code slightly outperforms the XYZ planar code. This is due to the fact that the threshold of the standard planar code steadily decreases with increasing bias, dropping to about 10.8% at $\eta = 10$, while the XYZ planar code exhibits a more complex behavior. For $\eta \in \{0.5, 1, 3, 10, 30, 100, 300, 1000, \infty\}$, the thresholds of the XYZ planar code are 0.1477(4), 0.1554(6), 0.1419(2), 0.1419(5), 0.1421(1), 0.1424(4), 0.1423(2), 0.1420(2) and 0.1425(6), respectively. Figure 4 presents the estimated failure rates f for representative biases $\eta \in \{1, 10, 100, 1000\}$ across various physical error rates p and code distances d , along with the scaled data as a function of x . Visual inspection confirms good qualitative agreement with the model.

The complex threshold behavior of the XYZ planar code can be attributed to two competing factors. On one hand, as bias increases, the density of nodes in the Z -check subgraphs grows, which affects the XYZ planar code in a manner similar to the standard planar code under MWPM decoding. On the other hand, the adverse impact of X or Y errors on the reweighting process is more pronounced at low bias. As bias increases, the occurrence of bit-flip errors decreases, allowing the pMWPM decoder to leverage its

advantages more effectively. However, the simultaneous increase in the density of the Z -check subgraphs introduces additional challenges for the decoder. Figure 5 provides an example supporting the above statement. When using pMWPM decoding for the XYZ planar code without changing the density of the Z -check subgraphs, moderately increasing the X or Y error rates raises the logical X error rate. Moreover, larger-distance codes are more susceptible to this change than smaller-distance codes, and the logical X error rate, which originally decreases with increasing d , turns to increase with d .

For a fixed physical error rate of 10%, the logical error rates of the XYZ planar code decoded with pMWPM and the standard planar code decoded with MWPM are compared under various biases. The comparison results are shown in Figure 6. To obtain logical error rate results with low overall statistical uncertainty, the above comparison is performed using smaller code distances d . The red curve corresponds to the standard planar code with MWPM decoding, and the blue curve to the XYZ planar code with pMWPM decoding. It can be observed that the decoding performance of the latter is significantly better than that of the former, representing a substantial improvement achieved at the cost of only a very slight increase in complexity.

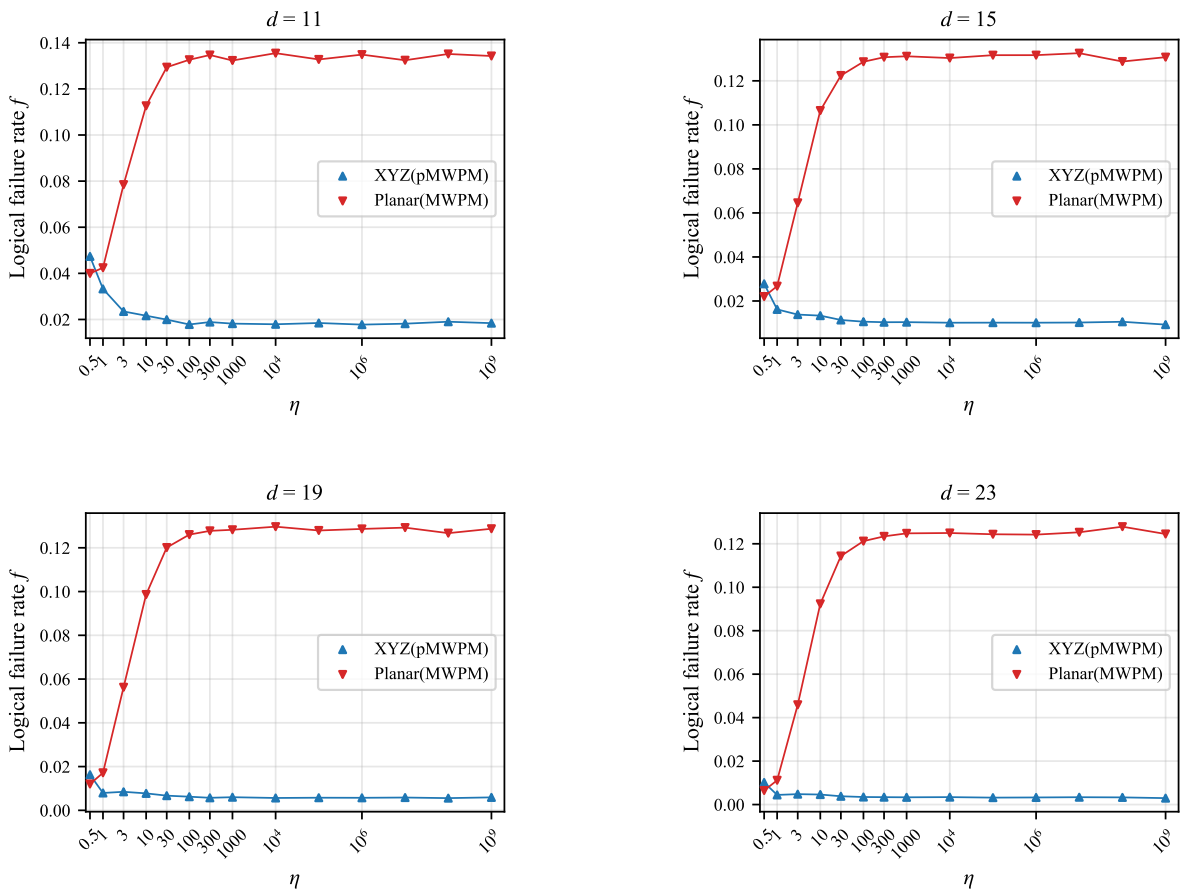


Figure 6: Logical failure rate as a function of Z -error bias for a physical error probability of 10%, for the XYZ planar code and the standard planar code with distances 11, 15, 19, and 23. The red curve represents the error probability of the standard planar code decoded using the MWPM decoder, while the blue curve shows the performance of the XYZ planar code decoded using the pMWPM method.

7 SIMULATIONS

All simulations in this paper were performed using the PyMatching package [12]. For the threshold calculation, square lattices with code distances $d \in \{35, 39, 43, 47\}$ are used for finite biases $\eta = 1/2, 1, 3, 10, 30, 100, 1000$ and for infinite bias $\eta = \infty$. For each code distance and each error rate, data are obtained via 10^5 Monte Carlo samplings. For each code distance, the errors are retained to four significant figures using jackknife resampling. Experiments are also performed for various biases at a

fixed physical error rate using code distances $d \in \{11, 15, 19, 23\}$. For each code distance and each error rate, data are obtained via 10^5 Monte Carlo samplings.

8 CONCLUSION

In this paper, a variant of the planar code is proposed by replacing all Z -measurement qubits with ZY -measurement qubits, resulting in a new XYZ planar code. An improved decoding algorithm, termed a posteriori minimum-weight perfect matching, is also designed. It is demonstrated that the measurement results of the ZY -measurement qubits can be used to reassess the probability of a Z error occurring on a specific data qubit. After reweighting, MWPM is performed. With only a slight increase in complexity, the decoding performance is significantly enhanced. Simulation results show that the threshold of the XYZ planar code exceeds that of the planar code for the vast majority of bias values considered in the experiments ($\eta \geq 10$), with an improvement of at least 30%. The main conclusion is that the XYZ planar code can significantly improve decoding performance under almost all biased noise channels compared to the planar code decoded with MWPM, at the cost of only a modest increase in complexity. In this paper, the analysis is restricted to the XYZ planar code; however, by adjusting the subgraph structure and the special arrangement of ZY stabilizers, the method can be easily extended to toric codes and rotated planar codes. Furthermore, by varying the number of Y operators, a variety of different XYZ surface codes can also be generated. The assigned weight values can be precomputed individually based on independent structures that may be assumed to be of arbitrary size, and the limiting case of this construction is the XY surface code [6].

Previous studies have optimized MWPM by reweighting the edges of the subgraphs. In [27, 37], the correlation between the X -check subgraphs and Z -check subgraphs was considered, based on the fact that a Y error is a combination of X and Z errors, and the information from one subgraph is used to reweight the other. In [16], edge weights were adjusted using probabilities obtained from a prior belief propagation (BP) process. The structure of the XYZ code enables its specialized decoder to more fully exploit the information from both subgraphs to jointly decode Z errors, and this process needs to be performed only once. In contrast, recursive MWPM continuously updates both subgraphs until they converge to the same error estimate [27].

Furthermore, simulation results provide an example supporting the following statement: for the XYZ planar code, although pMWPM enhances the decoding capability for the Z -check subgraph, it is adversely affected by X or Y errors, which is unavoidable when pMWPM attempts to utilize the measurement outcomes of ZY stabilizer measurements. This explains why the threshold does not increase monotonically with bias; instead, the highest threshold is achieved near $\eta = 1$. Over the wide range of biases examined, the threshold remains between 14% and 16%, reflecting the robustness of the XYZ planar code under different bias values. Moreover, for fixed code distance and physical error rate, the logical failure rate of the XYZ planar code is significantly lower than that of the planar code.

The data and code supporting the findings of this study are available from the corresponding author upon reasonable request.

9 ACKNOWLEDGMENTS

We are grateful to the anonymous referees and the associate editor for useful comments and suggestions that improved the presentation and quality of this paper. The work was supported by the National Natural Science Foundation of China under Grant No. 12271137.

A APPENDIX: DERIVATION OF CONDITIONAL Z OR Y ERROR PROBABILITIES FOR THE CENTRAL QUBIT

The conditional probability that the central qubit (qubit 4) suffers a Z or Y error, given the two stabilizer measurement outcomes $S_1, S_2 \in \{0, 1\}$ (0 = trivial change; 1 = non-trivial change), is derived. Two configurations are considered: (i) 4-qubit stabilizers $Z_1 Z_2 Z_3 Y_4$ and $Z_5 Z_6 Z_7 Y_4$, where each group contains three peripheral qubits; and (ii) 3-qubit stabilizers $Z_2 Z_3 Y_4$ and $Z_5 Z_6 Y_4$, where each group contains two peripheral qubits. The derivation is identical in structure for both cases; only the parity probabilities E_n (even number of flips) and O_n (odd number of flips) differ.

Each data qubit independently suffers an error with probabilities p_x , p_y , p_z , and non-error with probability $p_i = 1 - p$, where $p = p_x + p_y + p_z$. For a given bias parameter η ,

$$p_x = p_y = \frac{p}{2(\eta + 1)}, \quad p_z = \frac{\eta p}{\eta + 1}. \quad (\text{A1})$$

For any peripheral qubit, an X or Y error flips its associated stabilizer measurement. Hence the probability that a given peripheral qubit causes a flip is $q = p_x + p_y$. Qubit 4 affects both stabilizer measurements simultaneously: an X or Z error flips both stabilizer measurements (call this state $t = 1$), while I (no error) or a Y error flips neither stabilizer measurement (state $t = 0$). Thus

$$P(t = 1) = p_{\text{flip}} = p_x + p_z, \quad P(t = 0) = p_{\text{noflip}} = p_i + p_y. \quad (\text{A2})$$

Let the first group of peripheral qubits adjacent to the first stabilizer contain n qubits, and let the second group also contain n qubits. Their flip counts are independent and identically distributed. Denote by A the number of errors that cause flips in the first group, and by B that in the second group. Both A and B follow a binomial distribution $\text{Bin}(n, q)$. Define the parity probabilities

$$E_n = P(\text{parity of } A \text{ is even}) = \sum_{k \text{ even}} \binom{n}{k} q^k (1-q)^{n-k}, \quad O_n = P(\text{parity of } A \text{ is odd}) = 1 - E_n. \quad (\text{A3})$$

For $n = 2$, the probabilities are $E_2 = (1-q)^2 + q^2$ and $O_2 = 2q(1-q)$. For $n = 3$, $E_3 = (1-q)^3 + 3q^2(1-q)$ and $O_3 = 3q(1-q)^2 + q^3$.

The measurement outcomes are determined by the parity of the peripheral flips and the state t of qubit 4:

$$S_1 = t \oplus (\text{parity of } A), \quad S_2 = t \oplus (\text{parity of } B), \quad (\text{A4})$$

where \oplus denotes addition modulo 2. Conditioned on t and the parities,

$$P(S_1 = s_1, S_2 = s_2 | t) = P(\text{parity}(A) = s_1 \oplus t) P(\text{parity}(B) = s_2 \oplus t). \quad (\text{A5})$$

For each possible error type on qubit 4, the joint probability with given outcomes can be written. If qubit 4 is idle (I , probability p_i) or has a Y error (probability p_y), then $t = 0$; if it has an X error (probability p_x) or a Z error (probability p_z), then $t = 1$. Consequently,

$$\begin{aligned} P(I, s_1, s_2) &= p_i P(\text{parity}(A) = s_1) P(\text{parity}(B) = s_2), \\ P(Y, s_1, s_2) &= p_y P(\text{parity}(A) = s_1) P(\text{parity}(B) = s_2), \\ P(X, s_1, s_2) &= p_x P(\text{parity}(A) = s_1 \oplus 1) P(\text{parity}(B) = s_2 \oplus 1), \\ P(Z, s_1, s_2) &= p_z P(\text{parity}(A) = s_1 \oplus 1) P(\text{parity}(B) = s_2 \oplus 1). \end{aligned} \quad (\text{A6})$$

Denote $P_{\text{even}} = E_n$ and $P_{\text{odd}} = O_n$.

Case $s_1 = s_2 = 0$. Here $P(\text{parity}(A) = 0) = E_n$ and $P(\text{parity}(A) = 1) = O_n$ (similarly for B). Thus

$$\begin{aligned} P(I, 00) &= p_i E_n^2, & P(Y, 00) &= p_y E_n^2, \\ P(X, 00) &= p_x O_n^2, & P(Z, 00) &= p_z O_n^2. \end{aligned} \quad (\text{A7})$$

The total probability of observing (00) is

$$P(00) = (p_i + p_y) E_n^2 + (p_x + p_z) O_n^2 = p_{\text{noflip}} E_n^2 + p_{\text{flip}} O_n^2. \quad (\text{A8})$$

The probability that qubit 4 has a Z or Y error and the outcome is (00) is $P(Z \cup Y, 00) = p_z O_n^2 + p_y E_n^2$. Hence

$$P(Z \cup Y | 00) = \frac{p_z O_n^2 + p_y E_n^2}{p_{\text{noflip}} E_n^2 + p_{\text{flip}} O_n^2}. \quad (\text{A9})$$

Case $s_1 = s_2 = 1$. Now $P(\text{parity}(A) = 1) = O_n$ and $P(\text{parity}(A) = 0) = E_n$. It follows that

$$\begin{aligned} P(I, 11) &= p_i O_n^2, & P(Y, 11) &= p_y O_n^2, \\ P(X, 11) &= p_x E_n^2, & P(Z, 11) &= p_z E_n^2. \end{aligned} \quad (\text{A10})$$

Thus

$$P(11) = (p_i + p_y) O_n^2 + (p_x + p_z) E_n^2 = p_{\text{noflip}} O_n^2 + p_{\text{flip}} E_n^2, \quad (\text{A11})$$

and $P(Z \cup Y, 11) = p_z E_n^2 + p_y O_n^2$. Therefore

$$P(Z \cup Y | 11) = \frac{p_z E_n^2 + p_y O_n^2}{p_{\text{noflip}} O_n^2 + p_{\text{flip}} E_n^2}. \quad (\text{A12})$$

Case $s_1 \neq s_2$. Without loss of generality, take $s_1 = 0, s_2 = 1$. Then $P(\text{parity}(A) = 0) = E_n$, $P(\text{parity}(B) = 1) = O_n$, $P(\text{parity}(A) = 1) = O_n$ and $P(\text{parity}(B) = 0) = E_n$. The following is computed:

$$\begin{aligned} P(I, 01) &= p_i E_n O_n, & P(Y, 01) &= p_y E_n O_n, \\ P(X, 01) &= p_x O_n E_n, & P(Z, 01) &= p_z O_n E_n. \end{aligned} \quad (\text{A13})$$

Hence

$$P(01) = (p_i + p_y) E_n O_n + (p_x + p_z) O_n E_n = (p_{\text{noflip}} + p_{\text{flip}}) E_n O_n = E_n O_n, \quad (\text{A14})$$

due to the fact that $p_{\text{noflip}} + p_{\text{flip}} = (p_i + p_y) + (p_x + p_z) = 1$. Moreover, $P(Z \cup Y, 01) = (p_z + p_y) E_n O_n$. Consequently,

$$P(Z \cup Y | 01) = \frac{(p_z + p_y) E_n O_n}{E_n O_n} = p_y + p_z. \quad (\text{A15})$$

By symmetry, the same result holds for $(s_1, s_2) = (1, 0)$. Thus

$$P(Z \cup Y | S_1 \neq S_2) = p_y + p_z, \quad (\text{A16})$$

which is exactly the prior probability $p_y + p_z$.

The posterior probabilities and weights for a range of physical error rates at $\eta = 1, 10, 100$, and 1000 are presented in Tables 1–4.

Table 1: Conditional probabilities and weights for $\eta = 1$.

p	$n = 2$			$n = 3$		
	$s_1 \neq s_2$	$s_1 = s_2 = 0$	$s_1 = s_2 = 1$	$s_1 \neq s_2$	$s_1 = s_2 = 0$	$s_1 = s_2 = 1$
0.02	0.015 000	0.005 080	0.649 402	0.015 000	0.005 085	0.629 061
0.04	0.030 000	0.010 343	0.633 145	0.030 000	0.010 385	0.595 856
0.06	0.045 000	0.015 824	0.617 865	0.045 000	0.015 969	0.566 542
0.10	0.075 000	0.027 598	0.590 138	0.075 000	0.028 299	0.517 928
0.12	0.090 000	0.033 979	0.577 642	0.090 000	0.035 208	0.497 952
0.14	0.105 000	0.040 752	0.566 028	0.105 000	0.042 728	0.480 491
0.16	0.120 000	0.047 968	0.555 278	0.120 000	0.050 945	0.465 315
0.18	0.135 000	0.055 682	0.545 371	0.135 000	0.059 942	0.452 224
0.20	0.150 000	0.063 949	0.536 293	0.150 000	0.069 796	0.441 046
Weights						
0.02	4.184 591	5.277 301	-0.616 413	4.184 591	5.276 285	-0.528 190
0.04	3.476 099	4.561 042	-0.545 731	3.476 099	4.556 935	-0.388 228
0.06	3.055 049	4.130 282	-0.484 098	3.055 049	4.120 981	-0.267 756
0.10	2.512 306	3.562 026	-0.364 536	2.512 306	3.563 236	-0.071 744
0.12	2.313 635	3.347 457	-0.313 100	2.313 635	3.310 635	0.008 193
0.14	2.142 863	3.158 657	-0.265 665	2.142 863	3.109 223	0.078 077
0.16	1.992 430	2.988 061	-0.222 018	1.992 430	2.924 714	0.138 965
0.18	1.857 455	2.830 805	-0.181 987	1.857 455	2.752 565	0.191 689
0.20	1.734 601	2.683 590	-0.145 427	1.734 601	2.589 833	0.236 919

References

- [1] A. Yu. Kitaev, Fault-tolerant quantum computation by anyons, *Ann. Phys.* **303**, 2 (2003).
- [2] S. B. Bravyi and A. Yu. Kitaev, Quantum codes on a lattice with boundary, arXiv:quant-ph/9811052 (1998).
- [3] P. Aliferis, F. Brito, D. P. DiVincenzo, J. Preskill, M. Steffen, and B. M. Terhal, Fault-tolerant computing with biased-noise superconducting qubits: A case study, *New J. Phys.* **11**, 013061 (2009).

Table 2: Conditional probabilities and weights for $\eta = 10$.

p	$n = 2$			$n = 3$		
	$s_1 \neq s_2$	$s_1 = s_2 = 0$	$s_1 = s_2 = 1$	$s_1 \neq s_2$	$s_1 = s_2 = 0$	$s_1 = s_2 = 1$
0.02	0.019 091	0.000 927	0.951 733	0.019 091	0.000 927	0.950 923
0.04	0.038 182	0.001 892	0.951 107	0.038 182	0.001 895	0.949 520
0.06	0.057 273	0.002 900	0.950 504	0.057 273	0.002 909	0.948 169
0.10	0.095 455	0.005 059	0.949 369	0.095 455	0.005 101	0.945 632
0.12	0.114 545	0.006 220	0.948 836	0.114 545	0.006 294	0.944 445
0.14	0.133 636	0.007 442	0.948 327	0.133 636	0.007 563	0.943 313
0.16	0.152 727	0.008 732	0.947 842	0.152 727	0.008 917	0.942 237
0.18	0.171 818	0.010 096	0.947 381	0.171 818	0.010 365	0.941 216
0.20	0.190 909	0.011 540	0.946 945	0.190 909	0.011 920	0.940 251
Weights						
0.02	3.939 268	6.982 597	-2.981 528	3.939 268	6.982 266	-2.964 052
0.04	3.226 466	6.268 031	-2.967 993	3.226 466	6.266 702	-2.934 369
0.06	2.800 952	5.840 175	-2.955 108	2.800 952	5.837 180	-2.906 553
0.10	2.248 782	5.281 559	-2.931 226	2.248 782	5.273 241	-2.856 078
0.12	2.045 129	5.073 793	-2.920 200	2.045 129	5.061 833	-2.833 228
0.14	1.869 182	4.893 134	-2.909 766	1.869 182	4.876 894	-2.811 860
0.16	1.713 369	4.732 007	-2.899 913	1.713 369	4.710 866	-2.791 906
0.18	1.572 796	4.585 514	-2.890 630	1.572 796	4.558 870	-2.773 304
0.20	1.444 114	4.450 305	-2.881 909	1.444 114	4.417 580	-2.755 997

Table 3: Conditional probabilities and weights for $\eta = 100$.

p	$n = 2$			$n = 3$		
	$s_1 \neq s_2$	$s_1 = s_2 = 0$	$s_1 = s_2 = 1$	$s_1 \neq s_2$	$s_1 = s_2 = 0$	$s_1 = s_2 = 1$
0.02	0.019 901	0.000 101	0.995 017	0.019 901	0.000 101	0.995 008
0.04	0.039 802	0.000 206	0.995 010	0.039 802	0.000 206	0.994 991
0.06	0.059 703	0.000 316	0.995 003	0.059 703	0.000 316	0.994 975
0.10	0.099 505	0.000 550	0.994 990	0.099 505	0.000 551	0.994 945
0.12	0.119 406	0.000 675	0.994 983	0.119 406	0.000 676	0.994 931
0.14	0.139 307	0.000 806	0.994 978	0.139 307	0.000 808	0.994 918
0.16	0.159 208	0.000 944	0.994 972	0.159 208	0.000 946	0.994 906
0.18	0.179 109	0.001 088	0.994 967	0.179 109	0.001 092	0.994 894
0.20	0.199 010	0.001 240	0.994 962	0.199 010	0.001 245	0.994 883
Weights						
0.02	3.896 884	9.200 057	-5.296 765	3.896 884	9.200 017	-5.294 829
0.04	3.183 223	8.486 196	-5.295 278	3.183 223	8.486 039	-5.291 492
0.06	2.756 814	8.059 520	-5.293 855	2.756 814	8.059 167	-5.288 304
0.10	2.202 737	7.504 707	-5.291 200	2.202 737	7.503 726	-5.282 374
0.12	1.998 068	7.299 567	-5.289 968	1.998 068	7.298 154	-5.279 629
0.14	1.821 058	7.122 017	-5.288 800	1.821 058	7.122 096	-5.277 029
0.16	1.664 133	6.964 484	-5.287 695	1.664 133	6.961 975	-5.274 573
0.18	1.522 396	6.822 068	-5.286 653	1.522 396	6.818 894	-5.272 261
0.20	1.392 494	6.691 418	-5.285 674	1.392 494	6.687 501	-5.270 092

Table 4: Conditional probabilities and weights for $\eta = 1000$.

p	$n = 2$			$n = 3$		
	$s_1 \neq s_2$	$s_1 = s_2 = 0$	$s_1 = s_2 = 1$	$s_1 \neq s_2$	$s_1 = s_2 = 0$	$s_1 = s_2 = 1$
0.02	0.019 990	0.000 010	0.999 500	0.019 990	0.000 010	0.999 500
0.04	0.039 980	0.000 021	0.999 500	0.039 980	0.000 021	0.999 500
0.06	0.059 970	0.000 032	0.999 500	0.059 970	0.000 032	0.999 500
0.10	0.099 950	0.000 056	0.999 500	0.099 950	0.000 056	0.999 499
0.12	0.119 940	0.000 068	0.999 500	0.119 940	0.000 068	0.999 499
0.14	0.139 930	0.000 081	0.999 500	0.139 930	0.000 081	0.999 499
0.16	0.159 920	0.000 095	0.999 500	0.159 920	0.000 095	0.999 499
0.18	0.179 910	0.000 110	0.999 500	0.179 910	0.000 110	0.999 499
0.20	0.199 900	0.000 125	0.999 500	0.199 900	0.000 125	0.999 499

Weights						
0.02	3.892 330	11.493 719	-7.600 746	3.892 330	11.493 715	-7.600 550
0.04	3.178 574	10.779 943	-7.600 596	3.178 574	10.779 927	-7.600 212
0.06	2.752 067	10.353 409	-7.600 452	2.752 067	10.353 373	-7.599 889
0.10	2.197 780	9.799 047	-7.600 183	2.197 780	9.798 947	-7.599 285
0.12	1.992 998	9.594 217	-7.600 059	1.992 998	9.594 073	-7.599 005
0.14	1.815 871	9.417 035	-7.599 940	1.815 871	9.416 840	-7.598 739
0.16	1.658 823	9.259 926	-7.599 829	1.658 823	9.259 670	-7.598 488
0.18	1.516 957	9.117 991	-7.599 723	1.516 957	9.117 667	-7.598 251
0.20	1.386 919	8.987 877	-7.599 624	1.386 919	8.987 478	-7.598 028

- [4] M. D. Shulman, O. E. Dial, S. P. Harvey, H. Bluhm, V. Umansky, and A. Yacoby, Demonstration of entanglement of electrostatically coupled singlet-triplet qubits, *Science* **336**, 202 (2012).
- [5] D. Nigg, M. Müller, E. A. Martinez, P. Schindler, M. Hennrich, T. Monz, M. A. Martin-Delgado, and R. Blatt, Quantum computations on a topologically encoded qubit, *Science* **345**, 302 (2014).
- [6] D. K. Tuckett, S. D. Bartlett, and S. T. Flammia, Ultrahigh error threshold for surface codes with biased noise, *Phys. Rev. Lett.* **120**, 050505 (2018).
- [7] D. K. Tuckett, A. S. Darmawan, C. T. Chubb, S. Bravyi, S. D. Bartlett, and S. T. Flammia, Tailoring surface codes for highly biased noise, *Phys. Rev. X* **9**, 041031 (2019).
- [8] J. P. Bonilla Ataides, D. K. Tuckett, S. D. Bartlett, S. T. Flammia, and J. B. Brown, The XZZX surface code, *Nat. Commun.* **12**, 2172 (2021).
- [9] A. Dua, A. Kubica, L. Jiang, S. T. Flammia, and M. J. Gullans, Clifford-deformed surface codes, *PRX Quantum* **5**, 010347 (2024).
- [10] J. Edmonds, Paths, trees, and flowers, *Can. J. Math.* **17**, 449 (1965).
- [11] A. G. Fowler, Minimum weight perfect matching of fault-tolerant topological quantum error correction in average $O(1)$ parallel time, *Quantum Inf. Comput.* **15**, 145 (2015).
- [12] O. Higgott, PyMatching: A Python package for decoding quantum codes with minimum-weight perfect matching, *ACM Trans. Quantum Comput.* **3**, 1 (2022).
- [13] O. Higgott and C. Gidney, Sparse blossom: Correcting a million errors per core second with minimum-weight matching, *Quantum* **9**, 1600 (2025).
- [14] Y. Wu and L. Zhong, Fusion blossom: Fast MWPM decoders for QEC, in *2023 IEEE International Conference on Quantum Computing and Engineering (QCE)* (IEEE Computer Society, Los Alamitos, CA, 2023), pp. 928–938.
- [15] N. Delfosse and N. H. Nickerson, Almost-linear time decoding algorithm for topological codes, *Quantum* **5**, 595 (2021).
- [16] O. Higgott, T. C. Bohdanowicz, A. Kubica, S. T. Flammia, and E. T. Campbell, Improved decoding of circuit noise and fragile boundaries of tailored surface codes, *Phys. Rev. X* **13**, 031007 (2023).

- [17] P. Panteleev and G. Kalachev, Degenerate quantum LDPC codes with good finite length performance, *Quantum* **5**, 585 (2021).
- [18] J. Roffe, D. R. White, S. Burton, and E. T. Campbell, Decoding across the quantum low-density parity-check code landscape, *Phys. Rev. Res.* **2**, 043423 (2020).
- [19] S. Bravyi, M. Suchara, and A. Vargo, Efficient algorithms for maximum likelihood decoding in the surface code, *Phys. Rev. A* **90**, 032326 (2014).
- [20] M. Herold, E. T. Campbell, J. Eisert, and M. J. Kastoryano, Cellular-automaton decoders for topological quantum memories, *npj Quantum Inf.* **1**, 15010 (2015).
- [21] A. Kubica and J. Preskill, Cellular-automaton decoders with provable thresholds for topological codes, *Phys. Rev. Lett.* **123**, 020501 (2019).
- [22] G. Duclos-Cianci and D. Poulin, Fast decoders for topological quantum codes, *Phys. Rev. Lett.* **104**, 050504 (2010).
- [23] C. Chamberland and P. Ronagh, Deep neural decoders for near term fault-tolerant experiments, *Quantum Sci. Technol.* **3**, 044002 (2018).
- [24] S. Varsamopoulos, B. Criger, and K. Bertels, Decoding small surface codes with feedforward neural networks, *Quantum Sci. Technol.* **3**, 015004 (2018).
- [25] L. Berent, L. Burgholzer, P. J. H. S. Derks, J. Eisert, and R. Wille, Decoding quantum color codes with MaxSAT, *Quantum* **8**, 1506 (2024).
- [26] A. deMarti iOlius, J. Etxezarreta Martinez, P. Fuentes, P. M. Crespo, and J. Garcia-Frías, Performance of surface codes in realistic quantum hardware, *Phys. Rev. A* **106**, 062428 (2022).
- [27] A. deMarti iOlius, J. Etxezarreta Martinez, P. Fuentes, and P. M. Crespo, Performance enhancement of surface codes via recursive minimum-weight perfect-match decoding, *Phys. Rev. A* **108**, 022401 (2023).
- [28] E. Dennis, A. Kitaev, A. Landahl, and J. Preskill, Topological quantum memory, *J. Math. Phys.* **43**, 4452 (2002).
- [29] B. M. Terhal, Quantum error correction for quantum memories, *Rev. Mod. Phys.* **87**, 307 (2015).
- [30] A. G. Fowler, M. Mariantoni, J. M. Martinis, and A. N. Cleland, Surface codes: Towards practical large-scale quantum computation, *Phys. Rev. A* **86**, 032324 (2012).
- [31] P. Padmanabhan, A. Chowdhury, F. Sugino, M. Guha Majumdar, and K. K. Sabapathy, Non-CSS color codes on 2D lattices: Models and topological properties, arXiv:2112.13617 (2021).
- [32] D. S. Wang, A. G. Fowler, A. M. Stephens, and L. C. L. Hollenberg, Threshold error rates for the toric and planar codes, *Quantum Inf. Comput.* **10**, 456 (2010).
- [33] A. deMarti iOlius, P. Fuentes, R. Orús, and P. M. Crespo, Review on the decoding algorithms for surface codes, *Quantum* **8**, 1180 (2024).
- [34] C. Wang, J. Harrington, and J. Preskill, Confinement-Higgs transition in a disordered gauge theory and the accuracy threshold for quantum memory, *Ann. Phys.* **303**, 31 (2003).
- [35] F. H. E. Watson and S. D. Barrett, Logical failure rate scaling of the toric code, *New J. Phys.* **16**, 093045 (2014).
- [36] Y. Xiao, B. Srivastava, and M. Granath, Exact results on finite size corrections for surface codes tailored to biased noise, *Quantum* **8**, 1468 (2024).
- [37] N. Delfosse and J. P. Tillich, A decoding algorithm for CSS codes using the X/Z correlations, in *2014 IEEE International Symposium on Information Theory* (IEEE, New York, 2014), pp. 1071–1075.